Design of High-Isolation Topological Duplexer Utilizing Dual-Edge State Topological Waveguides

Haolong Wang, Hongyu Shi, *Member, IEEE*, Wei E. I. Sha, *Senior Member, IEEE*, Zhihao Lan, Fei Gao, *Member, IEEE*, Xiaoming Chen, *Senior Member, IEEE*, and Anxue Zhang

***Abstract*— Topological edge states have gained significant attention due to their exceptional capability to transmit signals without being affected by defects, which make them promising for applications in microwave and terahertz integrated circuits. In this article, supercell structures based on topological photonics crystals (TPCs) under dual-edge state are proposed. The energy bands of the proposed supercells are different from those of traditional supercells in that they exhibit forbidden bandgaps in addition to edge state and bulk state, facilitating an effective out-of-band rejection filter function through the use of dual-edge state transmission. The robustness of this new structure against bends and fabrication defects has been experimentally validated. To demonstrate the feasibility of the proposed structure, we design and realize a topological duplexer, which delivers superior transceiver performance and exceptional isolation capabilities. The duplexer is configured with two distinct channels (first channel spanning from 13.20 to 13.43 GHz, while the second one ranging from 13.88 to 14.25 GHz), offering isolation of exceeding 27 dB and reaching up to 35 dB. The research findings offer flexible approaches for implementing frequency selection applications, serving as a reference for the future designs and application of integrated package duplexers.**

***Index Terms*— Duplexer, millimeter wave devices, topological edge state, topological photonic crystal (TPC), topological waveguide (TW).**

I. Introduction

TOPOLOGICAL waveguide (TW) devices composed of topological photonic crystals (TPCs) have garnered significant attention due to their unique transmission characteristics and potential applications [1], [2], [3]. Topological insulators are currently categorized into 1-D, 2-D, and higher order topological insulators [4]. At present, 2-D TPCs primarily include spin Hall effect-based TPCs [5], [6], [7], [8] and valley Hall effect-based TPCs [9], [10], [11], [12], [13]. Topological edge states can be induced by selectively combining different types of TPCs. A major application of topological edge currents is the case of insulators of closed shape where the current flows at their boundary [14], [15]. Even in the presence of defects and sharp bends, these states exhibit topological protection and robustness [16], [17], [18]. In addition, there are ongoing discussions about nonlinear TPCs and discontinuous TPCs. From a theoretical perspective, it has been proposed that using nonlinear media can tailor bandgaps and achieve higher order topological protection [19], [20]. Discontinuous topological structures, such as those sandwiched between two metallic surfaces, are also employed in antennas and waveguides, offering significant potential for terahertz and optical communications [21], [22], [23]. TPCs and TWs are widely utilized in numerous electromagnetic device applications, including optical switches [24], wavelength division multiplexers [25], [26], [27], [28], [29], lasers [30], frequency converters [31], antennas [32], [33], and beyond.

At present, a range of duplexers utilizing TPCs and demonstrating frequency-selective properties have emerged [25], [26], [27], [28], [29]. In [28], a duplexer achieving approximately 20-dB isolation has been demonstrated; however, it has a significant insertion loss of 10 dB (approximately), indicating low transmission efficiency. Another optimized duplexer discussed in [25] has been developed using topology optimization algorithms to achieve high transmission efficiency but features a relatively narrow bandwidth of approximately 1.5%. In [29], a duplexer utilizing tunable edge states has exhibited an insertion loss ranging from 7 to 10 dB, along with a common but not high isolation of up to 24.9 dB. The bottleneck in achieving high isolation, low insertion loss, and wide bandwidth simultaneously in the aforementioned devices stems from the energy band characteristics of TWs and the complexities involved in designing devices utilizing them. For TWs, the bulk state does not fully confine electromagnetic wave transmission, limiting isolation to 10–20 dB. In contrast, higher isolation is achievable within the forbidden bandgap. Therefore, the key to enhancing isolation is designing supercells with distinct forbidden bandgaps. Moreover, most

Received 3 June 2024; revised 17 August 2024; accepted 3 September 2024. Date of publication 17 September 2024; date of current version 30 October 2024. This work was supported in part by Shaanxi S and T Innovation Team under Grant 2023-CX-TD-03. *(Corresponding author: Hongyu Shi.)*

Haolong Wang and Hongyu Shi are with the MOE Key Laboratory for Multifunctional Materials and Structures, Xi'an Jiaotong University, Xi'an 710049, China (e-mail: wang1974@stu.xjtu.edu.cn; hongyushi@xjtu.edu.cn).

Wei E. I. Sha and Fei Gao are with the State Key Laboratory of Modern Optical Instrumentation, College of Information Science and Electronic Engineering, Zhejiang University, Hangzhou 310027, China (e-mail: weisha@zju.edu.cn; gaofeizju@zju.edu.cn).

Zhihao Lan is with the Department of Electronic and Electrical Engineering, University College London, WC1E 6BT London, U.K. (e-mail: lanzhihao7@gmail.com).

Xiaoming Chen and Anxue Zhang are with the School of Information and Communications Engineering, Xi'an Jiaotong University, Xi'an 710049, China (e-mail: xiaoming.chen@mail.xjtu.edu.cn; anxuezhang@mail.xjtu.edu.cn).

Color versions of one or more figures in this article are available at https://doi.org/10.1109/TAP.2024.3458399.

Digital Object Identifier 10.1109/TAP.2024.3458399

existing TWs suffer from low excitation efficiency due to their specific excitation needs, which typically involve chiral sources carrying phase vortices. This limitation restricts their practical applicability across diverse domains [21], [34], [35], [36], [37], [38]. Hence, there is an urgent necessity to enhance TWs by improving the frequency selectivity and in-band flatness of constituent supercells as well as by developing more efficient excitation methods [39], [40].

In this article, design of a topological duplexer characterized by high isolation and high transmission efficiency is presented. A distinctive TW is introduced based on the dual-edge state achieved by altering the arrangement way of TPCs. The energy bands of the constituent supercells in this TW exhibit forbidden bandgap in the high-frequency region. The forbidden bandgap enables the TW to achieve exceptionally high out-of-band rejection, reaching up to 35 dB in the forbidden bandgap region. The dimensions of TPCs can modify the widths of their energy bandgap. Leveraging this, another TW that operates in the high-frequency range is devised. A phase-shifting TPC within the dual-edge state TW is introduced to further enhance the isolation between the two ports and reduce insertion loss. The proposed duplexer features a low-frequency passband spanning from 13.20 to 13.40 GHz and a high-frequency passband ranging from 13.90 to 14.20 GHz. Its insertion loss is minimized to 0.5 dB in the passband while maintaining a maximum threshold of 1.0 dB, whereas isolation exceeding 25 dB and reaching up to 35 dB is achieved. The proposed duplexer based on a TW structure can be efficiently and directly excited using microstrip lines, supported by its low return loss of less than −12 dB. The duplexer was fabricated and tested, and the measurement results are consistent with the numerical simulations. The proposed design is shown to significantly enhance the supercell energy band characteristics, promising substantial advancements in on-chip microwave devices.

II. Dual-Edge State Transmission and Structure Design of TWs

The topological duplexer is designed utilizing the hexagonal TPC unit arranged with C3 symmetry. By adjusting the dimensions and arrangements of the TPC units, TW configurations with different frequencies and bandwidths can be achieved. Subsequently, two TWs with distinct passbands are integrated at two ports to fulfill the duplexer function. The TPC units' physical functioning relies on the quantum valley Hall effect [35], [41], [42]. Within the bandgap, TPCs with two different orientations exhibit opposite Chern numbers. According to the bulk-edge correspondence principle, transmission between the domain walls is made possible through topological edge states [10], [33], [43].

A. Dimension Parameters and Energy Band Properties of TPCs

The prototype design of the valley TPC is depicted in Fig. 1(a). With a lattice constant (a) of 5.6 mm, each TPC unit is a regular hexagon made up of six metal grid lines that have a width of w and one hexagonal metal patch. The

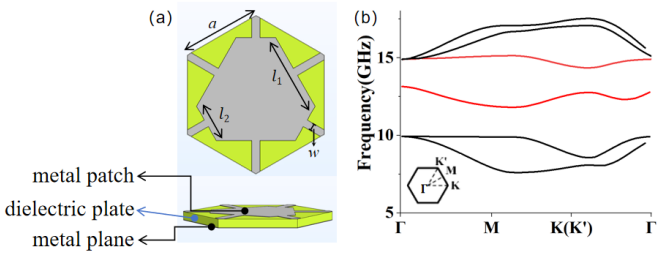

Fig. 1. (a) Prototype design and (b) energy band of TPC. The red lines represent the energy band lines of the Dirac point that was opened in the K(K') valley.

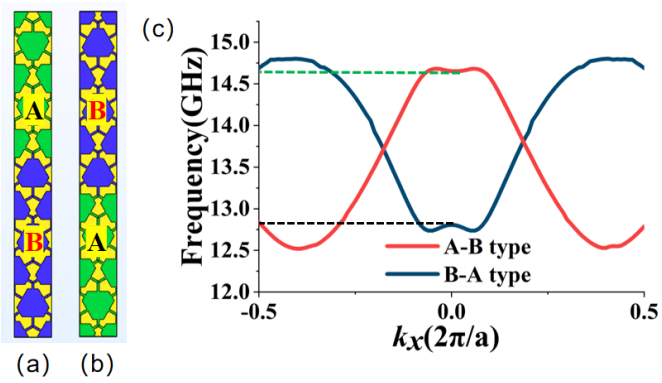

Fig. 2. Structures and energy bands of two types of supercells. (a) A-B type. (b) B-A type. (c) Energy bands of two types of supercells.

hexagonal metal patch exhibits C3 symmetry and features two sides of different lengths, l_1 and l_2 [35]. The energy band of a single TPC unit is illustrated in Fig. 1(b). The TPC characterized by C3 symmetry opens a Dirac cone at the K/K' valley, resulting in the formation of an energy bandgap [as depicted by the red line in Fig. 1(b)], spanning from 13.0 to 14.7 GHz. This type of TPC is labeled as Size I ($l_1 = 1.0 * a$, $l_2 = 0.5 * a$, and $w_1 = 0.1 * a$). The architectures of A-B-type and B-A-type supercell configurations are shown in Fig. 2(a) and (b), whereas the energy bands of these two structures are depicted in Fig. 2(c). Type A-B refers to the configuration where the narrow sides of the TPCs face each other, known as the face-to-face type. Conversely, Type B-A refers to the configuration where the wide sides of the TPCs face each other, known as the back-to-back type. In addition, the valley Hall edge states within the energy bandgap of the two types of supercell structures are shown in Fig. 2(c). The metal grid structure facilitates direct excitation of microstrip lines applied to the domain walls of TWs. Specific details are reported in [35].

B. Dual-Edge State Transmission and Low-Frequency TW Structure Design

A unique supercell structure with multiple layers of B-type TPCs and a single layer of A-type TPCs positioned centrally among the B-type layers is proposed to realize low-frequency TWs. The unique structure of the supercell is named dual-edge supercell and depicted in Fig. 3(a). Following energy band

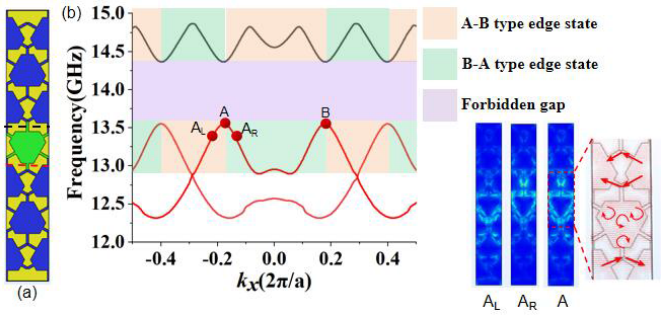

Fig. 3. Structure and characteristics of the proposed supercell with dual-edge state transmission. (a) Supercell structure with red dashed lines denoting A-B domain walls and black dashed lines representing B-A domain walls. (b) Energy band diagram of the supercell, where the purple region indicates the forbidden bandgap, while the green and pink regions depict the dual-edge state transmission range. Some of the energy band lines of the trivial mode are hidden. The green region represents eigenmodes where the energy flux mainly is confined in B-A-type domain, whereas the pink region signifies those where the energy flux is confined in A-B-type domain. Points A and B denote positions on the energy band peak located between the edge state and the forbidden bandgap. Furthermore, points A and B are positioned in the K' and K valleys, respectively. The electric field distributions of the eigenmodes at points A, A_L, and A_R are displayed in the bottom right. The time-mean power flux distribution diagram at point A is displayed with red arrows.

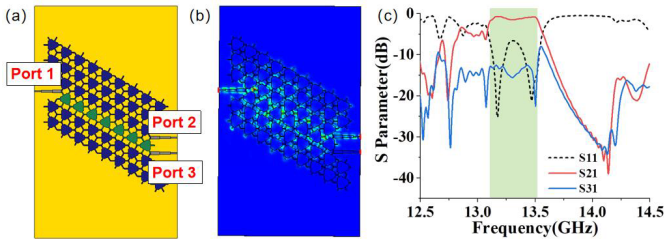

Fig. 4. TW structure comprised of supercells featuring dual-edge state transmission and its transmission performance. (a) Structure of dual-edge state TW. (b) Electric field distribution of the TW at Port 1 feeding (13.3 GHz). (c) S-parameter of the dual-edge state TW. The green region depicts the TW's passband.

scanning simulation using COMSOL, the energy band is presented in Fig. 3(b). This dual-edge supercell structure exhibits a forbidden bandgap ranging from 13.6 to 14.2 GHz [highlighted in purple in Fig. 3(b)]. An electric field transmission mode, termed the dual-edge state, closely resembling the edge state transmission mode within the supercell, emerges within the frequency range of 13.0–13.6 GHz, depicted by the green and pink colored segments in Fig. 3(b). Two distinct types of edge state transmission occur within the dual-edge supercell structure due to different TPC orientations in the middle layer. These transmissions are represented in Fig. 3(a) as B-A-type transmission on the top side (domain walls denoted by black dashed lines) and A-B-type transmission on the bottom side (domain walls represented by red dashed lines).

Points $A(k_x = -0.18)$ and $B(k_x = 0.18)$ represent two points of the highest frequencies of the energy band between the dual-edge state and the forbidden bandgap in the K' and K valleys, respectively. The energy band diagram at the bottom-right corner of Fig. 3(b) illustrates the eigenmode of point A. At point A, an edge state transmission mode is present in the domain walls on both sides of the interlayer B-type TPCs, where the electric field is focused. In this structure, these two edge states propagate in opposite directions in the K and K' valleys. As a result, multiple energy flux vortices are generated in the interlayer TPCs and are illustrated in the mean power flux distribution diagram at point A. This result agrees with the transmission characteristics of A-B-type and B-A-type edge states as inferred from the analysis of single-edge states [35].

To understand the mechanism of the dual-edge state, the transmission modes of the edge states around peak point $A(k_x = -0.18)$ at 13.63 GHz are examined, as shown in Fig. 3(b). In particular, the electric field eigenmodes at selected points within the passband range on both sides of point A are observed and are denoted as $A_L(k_x = -0.22)$ and $A_R(k_x = -0.14)$ in Fig. 3(b). In the close proximity to the left-hand side of point A, the dual-edge state concentrates the energy flux in the bottom side of the interlayer TPCs (A-B-type edge state). In contrast, in close proximity to the right-hand side of point A, the dual-edge state directs the energy flux toward the top side of the interlayer TPCs (B-A-type edge state). We observe the other eigenmodes in the energy band that are in the dual-edge state and get the conclusion, as shown in Fig. 3. The pink and green segments denote the regions where energy flux concentrates in the A-B and B-A domain walls, respectively. The energy band diagrams in Figs. 2 and 3(b) clearly show that the dual-edge state's energy band arises from a combination of the A-B and B-A edge state forms. Within the frequency range of 12.9–13.6 GHz, the weak interaction and diffusion between these edge states cause alternating dominance when the wave vector traverses through the corresponding positions. This leads to the formation of new energy bands within this frequency range. Within the frequency range of 13.6–14.2 GHz, the energy band structures of the two edge states exhibit a high degree of similarity, leading to a more pronounced mutual influence. Due to their opposite energy flux transmission directions, these states impose constraints and counterbalances on one another, resulting in the creation of a forbidden bandgap. Thus, the energy band illustrated in Fig. 3(b) facilitates effective filtering inside the forbidden bandgap, with the optimal passband ranging from 12.9 to 13.6 GHz.

After analyzing the energy band of the new supercell, the designed TW structure is utilized for low-frequency range filtering. The TW structure shown in Fig. 4(a) is simulated using Computer Simulation Technology (CST) software to observe the dual-edge state transmission and filtering effects. Upon exciting the TW through Port 1, energy flux is predominantly transmitted through the A-B domain wall. The constraints on energy flux at the B-A domain wall are imposed by valley momentum locking properties. The electric field of the TW at 13.3 GHz is illustrated in Fig. 4(b), whereas the S-parameters of the TW are shown in Fig. 4(c). It can be observed from Fig. 4(c) that the dual-edge state TW offers superior isolation in the high-frequency range, with S21 exceeding 25 dB and reaching a peak value of 38 dB between 13.8 and 14.2 GHz. It is evident that S21 significantly surpasses S31 in the passband, indicating a predominant energy flow toward Port 2

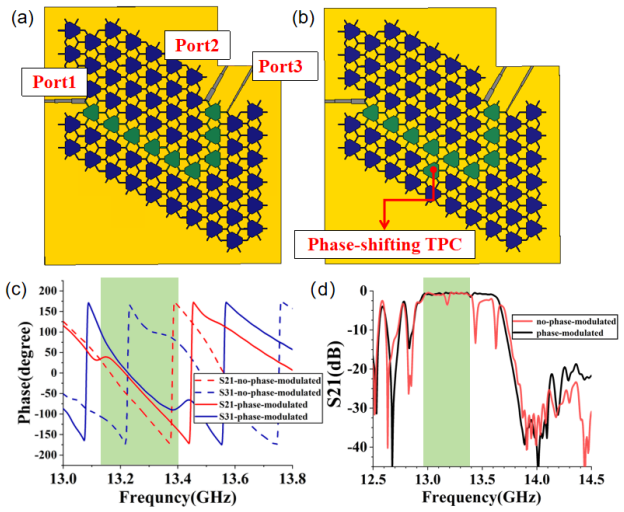

Fig. 5. Bending dual-edge state TWs to experimentally validate the function of the phase-shifting TPC. (a) Bending dual-edge state TW without phase-shifting TPC. (b) Bending dual-edge state TW with phase-shifting TPC. (c) Phase variation of the TWs. The dashed and solid lines represent the phase of TWs before and after the phase modulation. The red and blue lines represent S21 and S31 cases, while the green region indicates the low-frequency filtering range. (d) S21 of the TWs, where the red and black lines represent S21 of TWs before and after the phase modulation.

along the A-B-type domain wall. Port 3 receives minor energy coupling, with S31 maintained below −13 dB.

The experiment is devised to directly demonstrate the supercell's filtering capability. When the device is in operation, using the conventional TWs to excite one side of the dual-edge state instead of directly exciting with microstrip lines will reduce the return loss and guarantee a higher level of transmission efficiency. Furthermore, by adjusting the phase of the two energy paths in dual-edge state TWs, it is possible to mitigate energy loss. When there is only one output port in the device, coupling the energy from Port 3 to Port 2 necessitates phase synchronization between the two energy paths. To achieve the synchronization, it is necessary to modify the type of TPCs on Port 3. Two bending dual-edge state TWs with and without a phase-shifting TPC are created in the CST for testing, as depicted in Fig. 5(a) and (b). The phase results of these two TWs are depicted in Fig. 5(c) for comparison. It is to be noted that the dashed and solid lines indicate the phase of TWs before and after the phase modulation, whereas the red and blue lines correspond to S21 and S31. The green region signifies the low-frequency filtering range. Based on the results, it is evident that without the phase-shifting TPC, the phase difference between Ports 2 and 3 in the passband ranges from 90° to 120°. However, inclusion of phase-shifting TPC results in a substantial alteration of the phase of S31. As a result, the phase difference between the two ports is optimized to a range of only 5°–30°. The impact of phase-shifting TPC on insertion loss is illustrated in Fig. 5(d). At 13.18 GHz, S21 exhibited a depression when no phase-shifting TPC was added, which can be attributed to the phase difference between the two paths. This situation improved considerably following the use of phase-shifting TPC, which is evident from the reduced insertion loss at the output port and the improved in-band flatness.

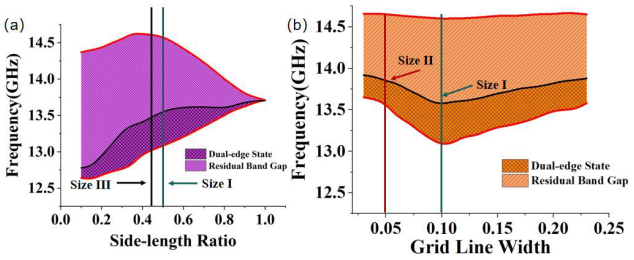

Fig. 6. Correlation between dimensions and energy bandwidths of TPCs. (a) Dual-edge state bandwidth versus side-length ratio, with the width of grid line set to $0.1 * a$. The purple region indicates the energy bandgap, whereas the darker shade represents the dual-edge state. The energy bands for supercells with TPCs of Size I and Size III are represented by green and black lines, respectively. (b) Dual-edge state bandwidth versus width of grid line, with side-length ratio fixed as 0.5. The orange region signifies the bandgap, whereas the darker shade represents the dual-edge state. The energy bands for supercells with TPCs of Size I and Size II are depicted in green and red lines, respectively.

C. Relationship Between Dimensions and Energy Bandwidths of TPCs

Prior research on TPCs has demonstrated that altering the dimensions of TPCs leads to changes in the energy bandgap [29], [44]. The TPCs studied in this article have adjustable dimensions, which include the lengths of the hexagon's sides (l_1 and l_2) and the width of the metal grid lines (w). It has been observed that altering the side-length ratio of hexagon (i.e., l_2/l_1, when $l_1 \geq l_2$) results in comparable changes in the bandwidth, as depicted in Fig. 6(a). In the figure, w is fixed at $0.1 * a$, and the purple region enclosed by the red line represents the energy band frequency range. As the side-length ratio of the two sides increases, the topological frequency window becomes narrower. This is due to the fact that as the side-length ratio decreases (when $l_2/l_1 \leq 1$), the spatial inversion symmetry of the TPC is disrupted to a greater extent, leading to increased degeneracy and, as a result, a larger bandwidth.

Furthermore, width of the grid lines (w) is an additional degree of freedom. The relationship between the energy bandgap width and the width of grid line, as shown in Fig. 6(b), depends on the side-length ratio of the hexagonal metal patch. In Fig. 6(b), the side-length ratio, l_2/l_1, is fixed at 0.5, and the orange region bounded by the red line represents the frequency range of energy band. Adjusting the width of grid line induces a shift in the low-frequency boundary [shown in blue in Fig. 6(b)] of the TPC energy bandgap. TPCs with $w = 0.05 * a$ are selected for the high-frequency channel, exhibiting a corresponding bandwidth range from 13.6 to 14.5 GHz, as indicated by the red line in Fig. 6(b). This type of TPC is designated as Size II ($l_1 = 1.0 * a$, $l_2 = 0.5 * a$, and $w_1 = 0.05 * a$).

The relationship between energy band characteristics and size remains consistent for supercell structure with dual-edge state. The regions shaded in dark below the black colored line in Fig. 6(a) and (b) represent the topological frequency window of the dual-edge state. The following are the key inferences: the frequency range of the dual-edge state aligns with the lower frequency range of the energy band of original topological edge state. As the side-length ratio decreases, the center frequency shifts to the lower frequency region.

Conversely, reducing the thickness of grid lines results in an increase in the shift of the center frequency. At the dimension changes, the frequency range of the dual-edge state will also change. In this study, TPCs with dimensions ($l_1 = 0.9 * a$, $l_2 = 0.4 * a$, and $w_3 = 0.1 * a$), called Size III, are employed to construct the dual-edge state TWs. The decreased side-length ratio of Size III TPC results in a broader bandwidth in the low-frequency range, improved in-band insertion loss, and out-of-band rejection due to better matching with the public port. TPCs with Size III are also selected considering factors, such as port matching, energy bandwidth, and transmission performance of TW.

D. Robustness Verification and High-Frequency TW Structure Design

A straight TW structure composed of Size I TPCs, connected directly with microstrip lines and excited by Port 1, is illustrated in Fig. 7(a). To evaluate the effectiveness of TWs in transmitting signals when there are sharp bends and manufacturing defects, a TW with two sets of Z-bending, as shown in Fig. 7(b), is considered. The simulation results of the S-parameters for both TWs are depicted in Fig. 7(c). Both TWs demonstrate comparable transmission performance within the passband ranging from 13.0 to 14.2 GHz. It can be seen that the TWs composed of TPCs of Size I have good bending robustness.

To verify the transmission performance and bending robustness of TWs composed of TPCs of Size II, both straight and curved TWs were designed using TPCs of Size II, following the structure depicted in Fig. 7(a) and (b). The S-parameters for these TWs exhibit comparable transmission performance in the frequency range of 13.5–14.3 GHz, as illustrated in Fig. 7(d). These are consistent with the energy bandwidths depicted in Fig. 6(b). Furthermore, the bending structure of the TW provides superior isolation in the low-frequency range, with the S21 values exceeding 24 dB and reaching up to 45 dB between 13.1 and 13.4 GHz. The aforementioned results indicate that the TWs of various diameters exhibit robustness against sharp bends when excitation by microstrip line.

Three common machining defects exist in TWs involving microstrip structures, namely, crystal defects, size disorder, and microstrip line loss. To evaluate the robustness of TWs to defects, these defects are introduced into the bent TW composed of TPCs with Size I, as illustrated in Fig. 8(a). Defect 1 corresponds to crystal breakages, defect 2 to size disorder, and defect 3 to microstrip line loss. The S-parameter results depicted in Fig. 8(b) demonstrated that these TWs exhibited a comparable transmission performance to that of the standard ones, indicating robustness against machining defects.

Similar to the traditional TWs, we also verify the topological robustness of the dual-edge TWs. On the basis of the dual-sided TW, two defects are added, respectively, as shown in Fig. 9(a). In the figure, defect 1 corresponds to crystal breakage, and defect 2 corresponds to size disorder. The S-parameter results depicted in Fig. 9(b) demonstrated that these TWs exhibited a comparable transmission performance to that of the standard ones, indicating robustness against machining defects.

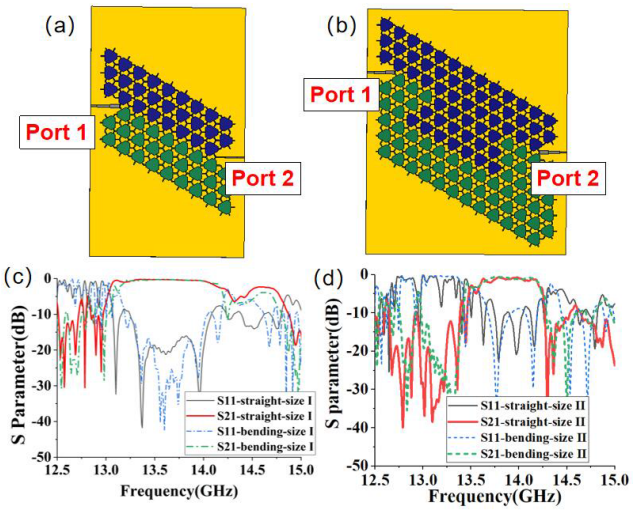

Fig. 7. TW structure and transmission performance in case of (a) straight TW structure and (b) Z-bending TW structure, (c) S-parameters of straight and Z-bending TWs composed of TPCs with Size I, and (d) S-parameters of straight and Z-bending TWs composed of TPCs with Size II.

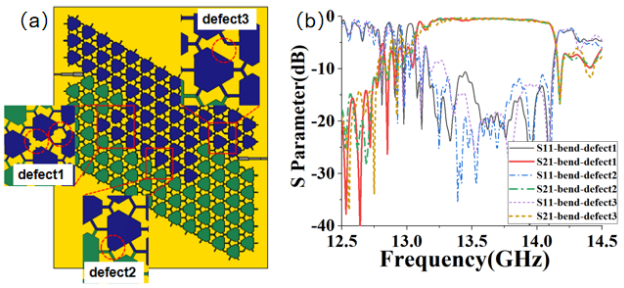

Fig. 8. Robustness of TW structure and transmission performance in case of (a) three structural defects designed on the Z-bending TW (defect 1 corresponds to crystal breakage, defect 2 corresponds to size disorder, and defect 3 corresponds to microstrip line loss) and (b) S-parameter corresponding to the defective TWs.

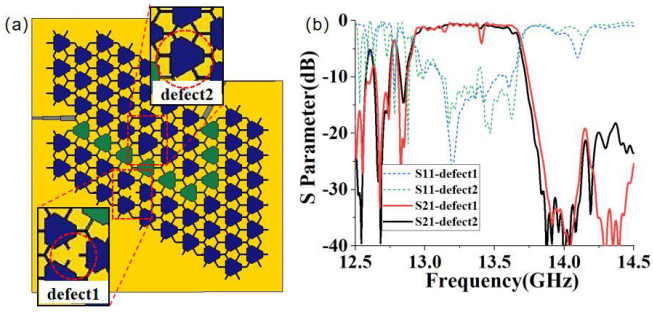

Fig. 9. Robustness of dual-edge state TW structure and transmission performance in case of (a) two structural defects designed on the bending dual-edge TW (defect 1 corresponds to crystal breakage and defect 2 corresponds to size disorder) and (b) S-parameter corresponding to the defective dual-edge TWs.

III. Topological Duplexer Implementation and Performance

A. Structure Design and Performance of Topological Duplexer

Based on the discussed principles, a three-port topological duplexer is designed, as shown in Fig. 10(a). Port 1 employs TPCs of Size I, represented by light blue (A-type) and light

green (B-type). Port 2 uses TPCs of Size II, represented by gray (A-type) and purple (B-type). Port 3 utilizes TPCs of Size III, represented by yellow (A-type) and dark green (B-type). Dual-edge state TWs are used for low-frequency channel, whereas TWs with TPCs of Size II are employed for high-frequency channel. The intersection point of duplexer is indicated by the brown dotted line, where the energy from the public port is divided into high- and low-frequency channels. The energy of different frequencies is routed into separate channels by TWs, ultimately reaching distinct ports. The microstrip lines are used to independently connect the three ports, with specific center frequencies and impedances. Ports 1–3 are connected to microstrip lines with the characteristic impedances of 32, 69.6, and 38 Ω. The quarter-wavelength converters ensure each port to a 50-Ω microstrip line, allowing for smooth integration with the device.

When operating in the low-frequency range, Ports 1 and 3 are active, effectively isolating Port 2. When Port 1 is excited, energy travels through the public channel indicated by black arrows. Upon reaching the intersection knot, energy travels down the low-frequency channel marked by red arrows, as illustrated in Fig. 10(a). The energy flux on the other path of the dual-edge state TW is unable to propagate downward because of the forbidden bandgap of high-frequency TW. A sharp bend in the low-frequency channel merges the energy edges, improving the insertion loss of Port 3. The electric field distribution has shown energy transmission from Port 1 to Port 3 at 13.3 GHz, which is depicted as red lines in Fig. 10(b).

At high frequencies, Ports 1 and 2 are active, effectively isolating Port 3. Energy transmission initially follows the public channel as shown by the black arrows. Upon reaching the intersection node, energy transmission follows through the high-frequency channel as indicated by blue arrows, as illustrated in Fig. 10(a). The low-frequency channel's TW prevents upward transmission, redirecting energy toward the high-frequency channel. Due to topological chiral spin locking, energy associated with the high-frequency channel is directed downward toward Port 2. The distribution of the electric field at a frequency of 14.0 GHz with Port 1 excited is illustrated in Fig. 10(c), which demonstrates the energy transmission from Port 1 to Port 2 along red lines. Fig. 10(e) shows the electric field intensity distribution near the three ports. The black square, red circle, and purple triangle represent Ports 1–3, respectively. Fig. 10(e) demonstrates that at 13.3 GHz, the device provides excellent isolation for Port 2. Similarly, at 14.0 GHz, it provides excellent isolation for Port 3.

The simulated S-parameters of the topological duplexer are shown in Fig. 10(d). The topological device and the microstrip line ports demonstrate excellent impedance matching, with a return loss in the passband as low as −12 dB. Findings from the simulations indicate that the low-frequency passband spans from 13.20 to 13.43 GHz, whereas the high-frequency passband ranges from 13.88 to 14.25 GHz. The insertion loss within both passbands ranges between 0.5 and 1.0 dB. The insertion loss at the frequencies of 13.38 and 14.09 GHz is precisely measured to be 0.5 and 0.6 dB, respectively. Furthermore, the level of isolation within the passbands is a minimum of 25 dB, reaching a maximum of 35 dB.

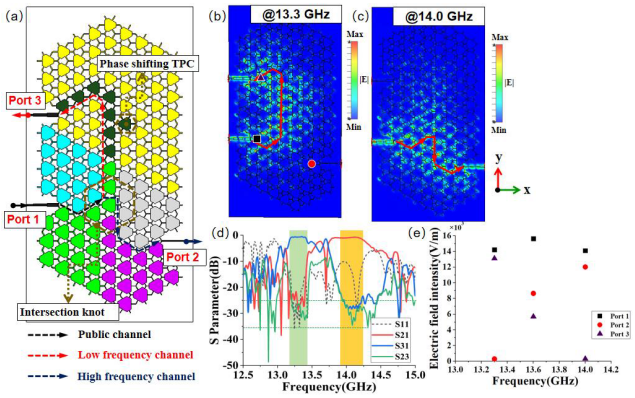

Fig. 10. Design of three-port topological duplexer, electric field distributions, and transmission performances. (a) Design drawing of the three-port topological duplexer, with dark blue dotted lines representing the high-frequency path and red dotted lines representing the low-frequency path. The intersection node of the duplexer and the phase-shifting TPC are marked by brown dotted line hexagons. (b) Electric field distribution diagram at 13.3 GHz. (c) Electric field distribution diagram at 14.0 GHz. (d) Simulated S-parameters of the duplexer. (e) Electric field intensity distribution of three ports at three different frequencies.

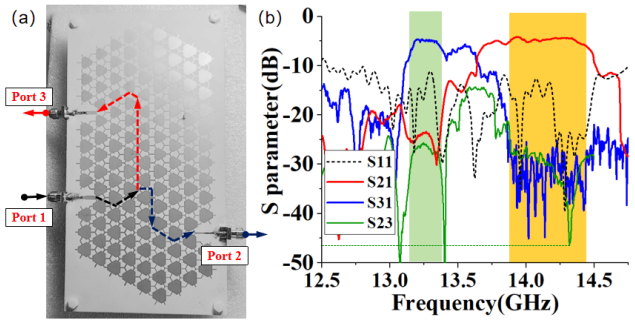

Fig. 11. (a) Photograph of the fabricated prototype of topological duplexer and (b) measured S-parameters of topological duplexer. The green region indicates the low-frequency band, whereas the yellow region represents the high-frequency band.

B. Experimental Results

The fabricated prototype of the topological duplexer in Fig. 10(a) is depicted in Fig. 11(a), whereas its transmission performance measured using vector network analyzer is shown in Fig. 11(b). The green and orange regions indicate the low- and high-frequency ranges, respectively. The measurements indicate that there is no frequency deviation from the expected frequency within the specified frequency range. The low-frequency passband extends from 13.20 to 13.40 GHz, while the high-frequency passband ranges from 13.80 to 14.45 GHz. The insertion loss varies from 3.8 to 5.4 dB, while the isolation surpasses 26 dB and can reach up to 46 dB within the passband.

Errors commonly arise during machining and measurements, including losses caused by the SMA interface and impedance mismatches due to port welding. Insufficient dielectric plate hardness leads to losses caused by bending deformation during measurement. While TWs are generally robust against defects, the presence of plate bending or unevenness can disrupt the symmetry of TPC, hence impacting the transmitting performance of all TWs.

IV. Conclusion

This article introduces the design of a high-isolation topological duplexer, employing valley TPCs that are directly excited by microstrip lines. By conducting thorough simulation and experimental studies, the duplexer is optimized by integrating three different types of 2-D TPCs with varying dimensions. First, a unique type of supercell is presented for transmitting under the dual-edge state, which facilitate a high out-of-band rejection. Furthermore, the analysis revealed the nuanced relationship between TPC dimensions and energy bandwidths, leading to the development of a high-frequency TW with robust out-of-band rejection. The designed duplexer demonstrated efficient connection and stimulation of microlines and TWs, validating their practical applications in microwave frequency and electromagnetism. Topological devices offer advantages over conventional on-chip devices due to their inherent immunity to defects and sharp bends. This study provides a foundational framework for future designs and applications, particularly in the areas of hybrid assemblies and integrated package duplexers.

References

[1] L. Lu, J. D. Joannopoulos, and M. Soljačić, "Topological photonics," *Nature Photon.*, vol. 8, pp. 821–829, Oct. 2014.

[2] A. B. Khanikaev and G. Shvets, "Two-dimensional topological photonics," *Nature Photon.*, vol. 11, no. 12, pp. 763–773, Dec. 2017.

[3] Y. Ruan et al., "Applications for wavelength division multiplexers based on topological photonic crystals," *Photon. Res.*, vol. 11, no. 4, p. 569, 2023.

[4] Z. Lan, M. L. N. Chen, F. Gao, S. Zhang, and W. E. I. Sha, "A brief review of topological photonics in one, two, and three dimensions," *Rev. Phys.*, vol. 9, Dec. 2022, Art. no. 100076.

[5] M. Hafezi, E. A. Demler, M. D. Lukin, and J. M. Taylor, "Robust optical delay lines with topological protection," *Nature Phys.*, vol. 7, no. 11, pp. 907–912, Nov. 2011.

[6] L.-H. Wu and X. Hu, "Scheme for achieving a topological photonic crystal by using dielectric material," *Phys. Rev. Lett.*, vol. 114, no. 22, Jun. 2015, Art. no. 223901.

[7] X. Cheng, C. Jouvaud, X. Ni, S. H. Mousavi, A. Z. Genack, and A. B. Khanikaev, "Robust reconfigurable electromagnetic pathways within a photonic topological insulator," *Nature Mater.*, vol. 15, no. 5, pp. 542–548, May 2016.

[8] Y. Yang et al., "Visualization of a unidirectional electromagnetic waveguide using topological photonic crystals made of dielectric materials," *Phys. Rev. Lett.*, vol. 120, no. 21, May 2018, Art. no. 217401.

[9] H. Xue, Y. Yang, and B. Zhang, "Topological valley photonics: Physics and device applications," *Adv. Photon. Res.*, vol. 2, no. 8, Aug. 2021, Art. no. 2100013.

[10] J. Ma, X. Xi, and X. Sun, "Topological photonic integrated circuits based on valley kink states," *Laser Photon. Rev.*, vol. 13, no. 12, Dec. 2019, Art. no. 1900087.

[11] X.-D. Chen, F.-L. Zhao, M. Chen, and J.-W. Dong, "Valley-contrasting physics in all-dielectric photonic crystals: Orbital angular momentum and topological propagation," *Phys. Rev. B, Condens. Matter*, vol. 96, no. 2, Jul. 2017, Art. no. 020202.

[12] F. Gao et al., "Topologically protected refraction of robust kink states in valley photonic crystals," *Nature Phys.*, vol. 14, no. 2, pp. 140–144, Feb. 2018.

[13] W.-S. Ruan, X.-T. He, F.-L. Zhao, and J.-W. Dong, "Analysis of unidirectional coupling in topological valley photonic crystal waveguides," *J. Lightw. Technol.*, vol. 39, no. 4, pp. 889–895, Feb. 15, 2021.

[14] S. A. Hassani Gangaraj, C. Valagiannopoulos, and F. Monticone, "Topological scattering resonances at ultralow frequencies," *Phys. Rev. Res.*, vol. 2, no. 2, May 2020, Art. no. 023180.

[15] Z. Z. Alisultanov and A. Kudlis, "Disorder-induced topological transitions in a multilayer topological insulator," *Phys. Rev. B, Condens. Matter*, vol. 109, no. 16, Apr. 2024, Art. no. 165141.

[16] Z. Wang, Y. Chong, J. D. Joannopoulos, and M. Soljačić, "Observation of unidirectional backscattering-immune topological electromagnetic states," *Nature*, vol. 461, no. 7265, pp. 772–775, Oct. 2009.

[17] X. Ni, S. Yves, A. Krasnok, and A. Alu, "Topological metamaterials," *Chem. Rev.*, vol. 123, pp. 7585–7654, Nov. 2022.

[18] R. Zhou et al., "Protected transverse electric waves in topological dielectric waveguides," *IEEE Trans. Antennas Propag.*, vol. 72, no. 2, pp. 2058–2063, Feb. 2024.

[19] D. Smirnova, D. Leykam, Y. Chong, and Y. Kivshar, "Nonlinear topological photonics," *Appl. Phys. Rev.*, vol. 7, no. 2, Jun. 2020, Art. no. 021306.

[20] J. Lu, L. He, Z. Addison, E. J. Mele, and B. Zhen, "Floquet topological phases in one-dimensional nonlinear photonic crystals," *Phys. Rev. Lett.*, vol. 126, no. 11, Mar. 2021, Art. no. 113901.

[21] M. L. N. Chen, L. J. Jiang, Z. Lan, and W. E. I. Sha, "Pseudospin-polarized topological line defects in dielectric photonic crystals," *IEEE Trans. Antennas Propag.*, vol. 68, no. 1, pp. 609–613, Jan. 2020.

[22] M. Y. Wang et al., "Underwater ultrasonic topological waveguides by metal additive manufacturing," *Appl. Phys. Lett.*, vol. 120, no. 14, Apr. 2022, Art. no. 141702.

[23] C. A. Valagiannopoulos, "High selectivity and controllability of a parallel-plate component with a filled rectangular ridge," *Prog. Electromagn. Res.*, vol. 119, pp. 497–511, 2011.

[24] X. Liu et al., "Terahertz topological photonic waveguide switch for on-chip communication," *Photon. Res.*, vol. 10, no. 4, p. 1090, 2022.

[25] K. Xu, Z. Xiao, X. Deng, G. Xie, M. Fang, and Z. Huang, "Topology optimization-based design of topological edge-state wavelength division multiplexer," *IEEE Photon. Technol. Lett.*, vol. 35, no. 14, pp. 773–776, Jul. 1, 2023.

[26] L. Zhang et al., "Valley kink states and topological channel intersections in substrate-integrated photonic circuitry," *Laser Photon. Rev.*, vol. 13, no. 11, 2019, Art. no. 1900159.

[27] X. Wu et al., "Direct observation of valley-polarized topological edge states in designer surface plasmon crystals," *Nature Commun.*, vol. 8, no. 1, p. 1304, Nov. 2017.

[28] G.-J. Tang, X.-D. Chen, F.-L. Shi, J.-W. Liu, M. Chen, and J.-W. Dong, "Frequency range dependent topological phases and photonic detouring in valley photonic crystals," *Phys. Rev. B, Condens. Matter*, vol. 102, no. 17, Nov. 2020, Art. no. 174202.

[29] X. Wang et al., "Design of wavelength division multiplexing devices based on tunable edge states of valley photonic crystals," *Opt. Exp.*, vol. 31, no. 9, p. 13933, Apr. 2023.

[30] Y. Zeng et al., "Electrically pumped topological laser with valley edge modes," *Nature*, vol. 578, no. 7794, pp. 246–250, Feb. 2020.

[31] K. A. Kuznetsov et al., "Terahertz radiation sources and frequency converters based on topological insulators," in *Proc. Int. Conf. Laser Opt. (ICLO)*, Jun. 2022, p. 1.

[32] Z. Zhang et al., "Directional acoustic antennas based on Valley-Hall topological insulators," *Adv. Mater.*, vol. 30, no. 36, Sep. 2018, Art. no. 1803229.

[33] Z. Xu, M. Wang, S. Fang, H. Liu, Z. Wang, and D. F. Sievenpiper, "Broadside radiation from Chern photonic topological insulators," *IEEE Trans. Antennas Propag.*, vol. 70, no. 3, pp. 2358–2363, Mar. 2022.

[34] X. Yu, J. Chen, Z.-Y. Li, and W. Liang, "Topological large-area one-way transmission in pseudospin-field-dependent waveguides using magneto-optical photonic crystals," *Photon. Res.*, vol. 11, no. 6, p. 1105, 2023.

[35] H. Shi et al., "A topological directional coupler fed by microstrip line with configurable coupling coefficient," *J. Lightw. Technol.*, vol. 41, no. 20, pp. 6542–6548, Oct. 15, 2023.

[36] X. He, X. Wang, Y. Zhao, R. Zhuo, and F. Liang, "Field programmable topological edge array," *Photon. Res.*, vol. 11, no. 3, p. 476, 2023.

[37] A. Kumar et al., "Phototunable chip-scale topological photonics: 160 Gbps waveguide and demultiplexer for THz 6G communication," *Nature Commun.*, vol. 13, no. 1, p. 5404, Sep. 2022.

[38] S. Keshavarz and D. L. Sounas, "Topological insulator metamaterials based on transmission line networks," in *Proc. IEEE Int. Symp. Antennas Propag. USNC-URSI Radio Sci. Meeting (AP-S/URSI)*, Jul. 2022, pp. 972–973.

[39] R. J. Davis, D. J. Bisharat, and D. F. Sievenpiper, "Classical-to-topological transmission line couplers," *Appl. Phys. Lett.*, vol. 118, no. 13, Mar. 2021, Art. no. 131102.

[40] X. Zhang, L. Wang, Y. Zhang, and Z. Yang, "Terahertz topological photonic integrated transmission line based on valley spin states," in *Proc. 24th Int. Vac. Electron. Conf. (IVEC)*, Apr. 2023, pp. 1–3.

[41] S. Li, M. L. N. Chen, Z. Lan, and P. Li, "Coexistence of large-area topological pseudospin and valley states in a tri-band heterostructure system," *Opt. Lett.*, vol. 48, no. 17, p. 4693, Sep. 2023.
[42] Q. Chen et al., "Photonic topological valley-locked waveguides," *ACS Photon.*, vol. 8, no. 5, pp. 1400–1406, May 2021.
[43] Q. Yan, "Quantum topological photonics," *Adv. Opt. Mater.*, vol. 9, no. 15, 2021, Art. no. 2001739.
[44] Y. Yang et al., "Terahertz topological photonics for on-chip communication," *Nature Photon.*, vol. 14, no. 7, pp. 446–451, Jul. 2020.

Haolong Wang was born in Jiangsu, China, in 2001. He received the B.S. degree in information and communication engineering from Xi'an Jiaotong University, Xi'an, China, in 2022, where he is currently pursuing the Ph.D. degree in electronic science and technology.

His current research interests include topological photonic crystal theory and topological device design.

Hongyu Shi (Member, IEEE) received the B.Sc. degree in electronic information science and technology from Dalian Maritime University, Dalian, China, in 2010, and the Ph.D. degree in electronic science and technology from Xi'an Jiaotong University, Xi'an, China, in 2015.

From 2015 to 2018, he was a Lecturer with Xi'an Jiaotong University. From 2018 to 2023, he was an Associate Professor with Xi'an Jiaotong University. Since 2024, he has been a Professor with Xi'an Jiaotong University, Xi'an. His research interests include metasurfaces theory and design, phased array antennas, and topological devices.

Wei E. I. Sha (Senior Member, IEEE) received the B.S. and Ph.D. degrees in electronic engineering with Anhui University, Hefei, China, in 2003 and 2008, respectively.

From July 2008 to July 2017, he was a Postdoctoral Research Fellow and then a Research Assistant Professor with the Department of Electrical and Electronic Engineering, University of Hong Kong, Hong Kong. From March 2018 to March 2019, he worked at University College London as a Marie Skłodowska-Curie Individual Fellow. From October 2017, he joined the College of Information Science and Electronic Engineering, Zhejiang University, Hangzhou, China, where he is currently a tenured Associate Professor. He has authored or co-authored 218 refereed journal papers, 182 conference publications (including seven keynote talks and three short courses), ten book chapters, and two books. His Google Scholar citation is 10 876 with an H-index of 55. His research interests include theoretical and computational research in electromagnetics and optics, focusing on the multiphysics and interdisciplinary research. His research involves fundamental and applied aspects in computational and applied electromagnetics, nonlinear and quantum electromagnetics, micro- and nano-optics, optoelectronic device simulation, and multiphysics modeling.

Dr. Sha is a life member of OSA. In 2015, he received Second Prize of Science and Technology from Anhui Province Government, China. In 2017, he received the Thousand Talents Program for Distinguished Young Scholars of China. He also received nine Best Student Paper Prizes and one Young Scientist Award with his students. He was a recipient of ACES-China Electromagnetics Education Ambassador Award 2024, ACES Technical Achievement Award 2022, and PIERS Young Scientist Award 2021. He served as Reviewers for 60 technical journals and Technical Program Committee Members of 10 IEEE conferences. He also served as an Associate Editor for IEEE JOURNAL ON MULTISCALE AND MULTIPHYSICS COMPUTATIONAL TECHNIQUES, IEEE OPEN JOURNAL OF ANTENNAS AND PROPAGATION, IEEE ACCESS, and *Electromagnetic Science*.

Zhihao Lan received the B.Sc. and M.Sc. degrees from Beijing Institute of Technology, and Peking University, Beijing, China, in 2004 and 2007, respectively, and the Ph.D. degree from Heriot-Watt University, Edinburgh, U.K., in 2012, all in physics.

He worked as a Post-Doctoral Research Fellow with Southampton University, Southampton, U.K., from 2011 to 2014, and Nottingham University, Nottingham, U.K., from 2014 to 2017. He joined the Department of Electronic and Electrical Engineering, University College London, London, U.K., in 2018, as a Research Associate in theoretical and computational modeling of quantum photonic materials and devices. His research interests include quantum optics, quantum gases, quantum many-body physics, quantum nonequilibrium systems, novel quantum systems for quantum simulations and quantum technologies, topological states of matter, topological photonics, and plasmonics.

Fei Gao (Member, IEEE) received the Ph.D. degree in physics and applied physics from Nanyang Technological University, Singapore, in 2016. He is now a tenured Associated Professor of the Department of Electrical Engineering, Zhejiang University, Hangzhou, China. His current research interests include metamaterials, topological electromagnetics, surface plasmons, and photonic crystals.

Xiaoming Chen (Senior Member, IEEE) received the B.Sc. degree in electrical engineering from Northwestern Polytechnical University, Xi'an, China, in 2006, and the M.Sc. and Ph.D. degrees in electrical engineering from the Chalmers University of Technology, Gothenburg, Sweden, in 2007 and 2012, respectively.

From 2013 to 2014, he was a Post-Doctoral Researcher with the Chalmers University of Technology. From 2014 to 2017, he was with Qamcom Research and Technology AB, Gothenburg, Sweden. Since 2017, he has been a Professor with Xi'an Jiaotong University, Xi'an. His research interests include multiple-input multiple-output (MIMO) antennas, over-the-air (OTA) testing, reverberation chambers, and electromagnetic information theory.

Prof. Chen received the Outstanding AE Awards six times from 2017 to 2023, and the International Union of Radio Science (URSI) Young Scientist Awards in 2017 and 2018. He serves as an Associate Editor for IEEE TRANSACTIONS ON ANTENNAS AND PROPAGATION and a Track Editor for IEEE ANTENNAS AND WIRELESS PROPAGATION LETTERS.

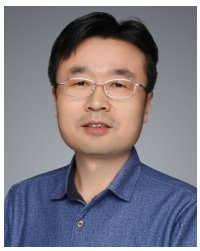

Anxue Zhang received the B.S. degree in electrical engineering from Henan Normal University, Henan, China, in 1996, and the M.S. and Ph.D. degrees in electrical engineering from Xi'an Jiaotong University, Xi'an, China, in 1999 and 2003, respectively.

He is currently a Professor and the Director of the Institute of Electromagnetics and Information Technology, Xi'an Jiaotong University. He has co-authored one book and more than 300 journal papers on his research topics. His research areas include antenna and electromagnetic wave propagation, RF and microwave circuit design, and metamaterials.

Dr. Zhang is a member of the Academic Committee of the Key Laboratory of Ultrahigh Speed Circuit Design and Electromagnetic Compatibility of the Ministry of Education.